



Contents lists available at ScienceDirect

Biochimica et Biophysica Acta

journal homepage: www.elsevier.com/locate/bbagen

Impact of surface grafting density of PEG macromolecules on dually fluorescent silica nanoparticles used for the *in vivo* imaging of subcutaneous tumors

Laurent Adumeau^a, Coralie Genevois^b, Lydia Roudier^a, Christophe Schatz^c,
Franck Couillaud^{b,*}, Stéphane Mornet^{a,**}

^a CNRS, Univ. Bordeaux, ICMCB, UPR 9048, F-33600 Pessac, France

^b Univ. Bordeaux, EA 7435 IMOTION - Imagerie moléculaire et thérapies innovantes en oncologie, 33706 Bordeaux, France

^c CNRS, Univ. Bordeaux, LCPO, UMR 5629, F-33600 Pessac, France

ARTICLE INFO

Article history:

Received 26 October 2016

Received in revised form 30 January 2017

Accepted 31 January 2017

Available online xxx

Keywords:

Nanoparticle

PEGylation

Tumor

EPR effect

Fluorescence imaging

in vivo

ABSTRACT

Background: In the context of systematically administered nanomedicines, the physicochemistry of NP surfaces must be controlled as a prerequisite to improve blood circulation time, and passive and active targeting. In particular, there is a real need to develop NP stealth and labelling for both *in vivo* and microscopic fluorescence imaging in a mice model.

Methods: We have synthesized NIR/red dually fluorescent silica nanoparticles of 19 nm covalently covered by a PEG layer of different grafting density in the brush conformational regime by using a reductive amination reaction. These particles were characterized by TEM, DRIFT, DLS, TGA, ζ potential measurements, UV-vis and fluorescence spectroscopy. Prostate tumors were generated in mice by subcutaneous injection of RM1-CMV-Fluc cells. Tumor growth was monitored by BLI after a D-luciferin injection. Four samples of PEGylated fluorescent NPs were individually intravenously injected into 6 mice ($N = 6$, total 24 mice). Nanoparticle distribution was investigated using *in vivo* fluorescence reflectance imaging (FRI) over 48 h and microscopy imaging was employed to localize the NPs within tumors *in vitro*.

Results: Fluorescent NP accumulation, due to the enhanced permeability and retention (EPR) effect, increases gradually as a function of increased PEG surface grafting density with a huge difference observed for the highest density grafting. For the highest grafting density, a blood circulation time of up to 24 h was observed with a strong reduction in uptake by the liver. *In vivo* experimental results suggest that the biodistribution of NPs is very sensitive to slight variations in surface grafting density when the NPs present a high curvature radius.

Conclusion: This study underlines the need to compensate a high curvature radius with a PEG-saturated NP surface to improve blood circulation and accumulation within tumors through the EPR effect. Dually fluorescent NPs PEGylated to saturation display physical properties useful for assessing the susceptibility of tumors to the EPR effect. **General significance:** Control of the physicochemical features of nanoparticle surfaces to improve blood circulation times and monitoring of the EPR effect. This article is part of a Special Issue entitled "Recent Advances in Bionanomaterials" Guest Editor: Dr. Marie-Louise Saboungi and Dr. Samuel D. Bader.

© 2017 Elsevier B.V. All rights reserved.

Abbreviations: NPs, nanoparticles; EPR, enhanced permeation and retention effect; i.v., intravenous; RES, reticuloendothelial system; PEG, polyethylene glycol; FRI, fluorescence reflectance imaging; NIR, near infra-red; TEOS, Tetraethyl orthosilicate; MPS, (3-mercaptopropyl)triethoxysilane; DL650, Dylight™650; DL800, Dylight™800; EDPS, N-[3-(trimethoxysilyl)propyl]ethylenediamine; DCM, dichloromethane; TFA, trifluoroacetic acid; DCC, dicyclohexylcarbodiimide; DMSO, dimethylsulfoxide; TEM, transmission electron microscopy; DLS, dynamic light scattering; DRIFT, Diffuse reflectance infrared Fourier transform; TGA, thermogravimetric analysis; BLI, bioluminescence imaging.

* Correspondence to: F. Couillaud, EA 7435 IMOTION, case 127, 146 rue Léo Saignat, 33706 Bordeaux, France.

** Correspondence to: S. Mornet, Bordeaux Institute of Condensed Matter Chemistry, 87 avenue du Dr. A. Schweitzer, Pessac F-33600, France.

E-mail addresses: franck.couillaud@u-bordeaux.fr (F. Couillaud), stephane.mornet@icmcb.cnrs.fr (S. Mornet).

1. Introduction

Determining the distribution of nanocarriers within the body upon systemic administration is one of the top priorities of nanomedicine [1]. In pursuit of this aim, there is a real need to develop labeled nanoparticles (NPs) to visualize the biodistribution in real time through imaging methods. Moreover, we must better understand the critical physicochemical parameters involved in the enhanced permeation and retention effect (EPR) of NPs [2,3]. Control over the physicochemical properties of NPs can determine the overall blood circulation kinetics [4], however, it is still hard to predict which type of NP can best estimate the susceptibility of the EPR effect in terms of the extravasation

<http://dx.doi.org/10.1016/j.bbagen.2017.01.036>

0304-4165/© 2017 Elsevier B.V. All rights reserved.

Please cite this article as: L. Adumeau, et al., Impact of surface grafting density of PEG macromolecules on dually fluorescent silica nanoparticles used for the *in vivo* imaging o..., Biochim. Biophys. Acta (2017), <http://dx.doi.org/10.1016/j.bbagen.2017.01.036>

processes and intratumoral diffusion. In addition, NPs as exogenous materials are liable to be eliminated by the immune defense system, which represents one of the major barriers for systematically administered nanomedicines. When NPs are administered, many plasma proteins called opsonins adsorb to the NPs surface, which are recognized by the scavenger receptor of the macrophage cell of the reticuloendothelial system (RES) [5]. An accurate control of these physicochemical features would allow us to better negotiate uptake and retention by the RES [6,7].

A way to prolong circulation of engineered nanoparticles is to develop anti-fouling strategies to reduce the effect of opsonization with plasma proteins. The gold standard to reduce non-specific protein adsorption and cellular uptake is to create a dense layer of polyethylene glycol (PEG) molecules on the nanoparticle surface (PEGylation). Many reviews have treated the topic concerning the interactions and circulation of PEGylated NPs in the blood, which depend on the influence of several key factors, including PEG molecular weight (MW), NP size, and PEG surface density [8–12]. Among these factors, the PEG surface grafting density on NPs is directly involved in the mechanism shielding against opsonins adsorption. It has been demonstrated that at a similar PEG grafting density, larger particles exhibit increased macrophage uptake compared to smaller NPs [13]. From these studies it also appears that to achieve stealth properties, there is a certain threshold of PEG surface density required far beyond the mushroom/brush transition [14]. The use of small NPs requires a higher PEG density to compensate for the spreading of flexible chains due to increased surface curvature. In this context, it seemed appropriate to address an *in vivo* study to highlight the impact on the EPR effect of slight variations in terms of PEG surface grafting density in the brush regime on highly curved NPs.

In the present study we synthesized fluorescent silica nanoparticles of 19 nm by incorporating near infra-red (NIR) and red fluorescent dyes to track their biodistribution *in vivo* over time by fluorescence reflectance imaging (FRI) and to check their localization in tumors by microscopic imaging. Four different levels of PEGylation grafting in the brush regime were produced by the use of a well-controlled surface chemistry. These PEGylated fluorescent NPs were injected intravenously in mice bearing subcutaneous tumors ($N = 6$, total 24 mice) in order to compare their accumulation in the liver and tumors through the EPR effect. After accurate quantification of PEG grafting density values by TGA analysis, the results are discussed in the light of recent reports [12–14].

2. Materials and methods

2.1. Chemicals

Tetraethyl orthosilicate (TEOS, 99.999%), (3-mercaptopropyl) triethoxysilane (MPS, 80% technical grade), N-[3-(trimethoxysilyl)propyl]ethylenediamine (EDPS, 97%), ammonium hydroxide solution (30%, ACS reagent), absolute ethanol (EtOH), glycerol (BioXtra, $\geq 99\%$), dichloromethane (DCM, anhydrous, $\geq 99.8\%$), trifluoroacetic acid (TFA, 99% reagent grade), pyridine (anhydrous, 99.8%), N,N'-dicyclohexylcarbodiimide (DCC, $\geq 99\%$ puriss.), petroleum ether (puriss., high boiling, bp 60–80 °C), isopropanol ($\geq 99.7\%$), poly(ethylene glycol) methyl ether (mPEG5k, Mn 5000 g/mol), sodium borohydride (NaBH_4 , 99.99%), methanol (MeOH, anhydrous, 99.8%) and triethylamine (Et_3N , $\geq 99.5\%$) were purchased from Sigma-Aldrich (Saint-Quentin Fallavier, France). Hydrochloric acid (37%, Normapur) was purchased from VWR (Fontenay-sous-Bois, France). Dylight™650-maleimide (DL650-mal, $\lambda_{\text{Ex}}/\lambda_{\text{Em}}$ 654/672 nm), Dylight™800-maleimide (DL800-mal, $\lambda_{\text{Ex}}/\lambda_{\text{Em}}$ 770/794 nm) and anhydrous dimethylsulfoxide (DMSO) were purchased from ThermoFisher Scientific, Illkirch, France). Sterile ultrapure water (18 M Ω) was produced using a SG-Labostar (7 TWF-UV) system from Odemi (Grisy, France). All materials were used as received, unless otherwise indicated.

2.2. Synthesis of dually fluorescent silica nanoparticles (DF-SiO₂NPs)

DL650-mal ($9.2 \cdot 10^{-7}$ mol, 1 eq., Thermo Scientific™) was dissolved in 100 μL of anhydrous DMSO. This fresh solution was added to 250 μL of absolute EtOH containing $3.68 \cdot 10^{-6}$ mol of 3-mercaptopropyl triethoxysilane (MPS, 4 eq.). The mixture was stirred for 2 h at room temperature in the dark. DL800-mal ($9.3 \cdot 10^{-7}$ mol, 1 eq.) was dissolved in 800 μL of anhydrous DMSO. This solution was added to a solution composed of 250 μL of absolute EtOH and $3.72 \cdot 10^{-7}$ mol of MPS (4 eq.). The mixture was stirred for 2 h at room temperature in the dark. Then, a solution composed of 37 mL of absolute EtOH, 762.5 μL of TEOS and the solutions of freshly prepared fluorescent silanes were rapidly added under continuous stirring to a solution composed of 99 mL of absolute EtOH, 3.7 mL of ammonia (30% w/w) and 0.4 mL of deionized water. The mixture was stirred for 12 h at room temperature in the dark. An additional thin silica layer was grown by adding 41 mL of deionized water and 550 μL of TEOS with a flow rate of 0.5 mL/h under gentle stirring. 4 h after the end of TEOS addition, ammonia was removed by evaporation under reduced pressure at 50 °C. The obtained nanoparticles are named DF-SiO₂NPs.

2.3. Surface modification of DF-SiO₂-NPs with an amino-silane coupling agent (DF-SiO₂NPs-EDPS)

The surface modification of colloidal silica was carried out according to reported methods [15–16]. Briefly, 1.7 mL of EDPS was added under vigorous stirring to disperse DF-SiO₂NPs representing 470 m² in developed surface area. After the overnight reaction under gentle stirring, a volume of 28 mL of glycerol was added and EtOH and water were removed under reduced pressure. Then the mixture was heated to 100 °C under vacuum for 1 h. Finally, excess EDPS and glycerol were removed through several washes (7 times with a dilution factor of about 15) with EtOH using tangential flow filtration using 300 kDa cutoff ultra-filtration filters (Merck Millipore). Then a few droplets (about 50 μL) of glacial acetic acid were added in order to favor the colloidal stabilization by protonation of amine groups. The washing was prolonged three times with anhydrous MeOH. The modified NPs named DF-SiO₂NPs-EDPS were stored in this form at room temperature in the dark ($\text{CSiO}_2 = 58.9$ g/L, estimated by dry weight).

2.4. Preparation of methoxypoly(ethylene glycol) acetaldehyde derivatives (mPEG5K-ald)

Aldehyde activated methoxypoly(ethylene glycol) (mPEG5K-ald) was produced by a metal-free Pfitzner-Moffatt oxidation according to modified procedures [17–19]. mPEG5K ($M_n = 5000$ g/mol, Fluka) (50 g, 10 mmol, 1 eq.) was dissolved in 65 mL of anhydrous DMSO. Traces of water were firstly removed by evaporation of 20 mL of DMSO under reduced pressure at 80 °C. After cooling to room temperature, 50 mL of anhydrous DCM were added. Pyridine (1.68 mL, 20 mmol, 2 eq.) and TFA (770 μL , 10 mmol, 1 eq.) were then added under stirring at 4 °C in an ice bath. After 30 min of stirring, DCC (12.4 g, 60 mmol, 6 eq.) was added and the mixture was kept in the ice bath for 20 h while stirring. The precipitate resulting from the dicyclohexylurea by-product was then removed by filtration at 4 °C. Thereafter, a cold solution of petroleum ether/propan-2-ol (4:1 vol%, 600 mL) was added in order to precipitate the mPEG5K-ald at -4 °C. The solid polymer was dissolved in 100 mL of dichloromethane, recrystallized using 500 mL of diethyl ether, recovered by filtration and dried under vacuum (weighing 43.5 g, yield 87%). The powder was stored at -20 °C.

2.5. Grafting of mPEG5K-ald on the surface of DF-SiO₂NPs-EDPS

Four batches were generated with various amount of mPEG5K-ald: Sample A corresponds to about a 22-fold excess of PEG-5k-ald macromolecules compared to the total primary amine functions exposed on

the NP surface, 2-fold excess for Sample B, stoichiometric conditions for Sample C and a 0.2 equivalent of PEG macromolecules for Sample D. Aliquots of 2.9 g, 0.29 g, 0.145 g and 0.029 g of mPEG5K-ald were diluted in 7.25 mL of anhydrous MeOH. Then, a volume of 849.2 μL of DF-SiO₂NPs-EDPS dispersion (corresponding to 50 mg for a total surface area of $\sim 7.89 \text{ m}^2$) was added dropwise while vigorously stirring each sample. After 5 min, a volume of 33.3 μL of Et₃N was added. The mixtures were protected from light and left to react for 4 h under reflux at 70 °C. Then a mass of 56 mg of NaBH₄ was added to each sample while stirring at room temperature and a volume of 1.5 mL of 1 M HCl was added 10 min later. The resulting samples of PEGylated NPs, were purified with ultrapure water by tangential flow filtration using 300 kDa cutoff filters. The washing step was achieved so as to obtain for each sample an identical concentration of residual free PEG chains of the order of 10^{-7} g/L . For instance, in a 10 mL filtration cell, the volume of sample A was reduced to 500 μL that gives a dilution factor of 20. This procedure was applied 6 times to reach a dilution factor of $6.4 \cdot 10^7$. Each PEGylated NP sample was suspended in a final volume of 4 mL to obtain stock solutions with a concentration of about 12.5 g/L in SiO₂. All dispersions were protected from light and stored at room temperature.

2.6. Physico-chemical properties of PEGylated DF-SiO₂ NPs

The size of nanoparticles was assessed by transmission electron microscopy (TEM). A volume of 5 μL of dispersed NPs was deposited on a carbon-film covered copper grid and allowed to adsorb for 1 min. The excess liquid was then removed using Whatman filter paper. TEM micrographs were performed with a Philips CM120 microscope operating at 120 kV and captured with an Ultra scan USC1000 2 k \times 2 k camera. NP size assessment was performed with Digital Micrograph software from Gatan.

The molar masses of mPEG5K and mPEG5K-ald were characterized by size-exclusion chromatography with a multiangle light scattering detection (WYATT, Dawn Heleos II) equipped with a JascoPU-980 pump and a differential refractive index detector (WYATT, Optilab rEX) in order to determine the average molecular weights (Mw) and dispersity (Mw/Mn). The ASTRA software (WYATT) controls the apparatus. The PEG molecules were analyzed in 0.01 M Na₂HPO₄/0.2 M NaNO₃, pH 9 using two columns from Shodex (OHpak SB-804 HQ) and a guard column. The flow rate was set to 0.6 mL/min and the injected volume was 100 μL . The dn/dc values were determined for each polymer with a differential refractive index detector (WYATT, Optilab rEX) in same buffer conditions as for the chromatographic elution.

¹H-NMR spectrum of mPEG5K-ald was performed in CDCl₃ with a Bruker NMR spectroscope working at 9.4 Tesla (400 MHz) (Spectrum shown in supplementary material document).

Hydrodynamic sizes and ζ potential were analyzed using a Zetasizer NanoZS from Malvern instruments (Worcestershire, UK) at various pH values, before and after being diluted by a factor of 2 with PBS buffer at 2 mg(SiO₂).L⁻¹. For dynamic light scattering (DLS) measurements, NP dispersions are systematically filtered with membrane disks with a 0.22 μm pore size (Durapore, Millipore).

Diffuse reflectance infrared Fourier transform (DRIFT) spectroscopy was performed with a Bruker IFS Equinox 55 FTIR spectrometer (signal averaging 32 scans at a resolution of 4 cm^{-1}) equipped by a selector Graseby Specac diffuse reflection cell (Eurolabo, France). A volume of the NP dispersion was dried at 80 °C under vacuum to obtain the sample in powder form. Then, samples were prepared by spreading crushed powders (3 wt%) in anhydrous (spectroscopy grade) KBr on a conical support.

For thermogravimetric analysis (TGA), 10 mg of nanoparticles, previously dried at 90 °C under a primary vacuum for 12 h, were placed in a platinum crucible, which was positioned on a Tag2400 thermobalance from Setaram (Caluire-et-Cuire, France). TGA measurements were consisted of a first temperature cycle from 25 °C to 650 °C by increasing

the heat by 2 °C/min under an Ar flux in order to favor the thermal decomposition of macromolecules in a short range of time. A second cycle (25–650 °C, 10 °C/min) was applied under an O₂ flux, heating up to 1000 °C to completely combust the organic matter. According to differentiated TGA diagrams, the surface grafting densities, σ , are assessed by subtraction of mass losses between 300 °C and 690 °C so as not to overestimate these values due to the remaining physisorbed water molecules at lower temperatures. Moreover, contributions of organic moieties of an aminated polysiloxane film, chemisorbed water and remaining ethoxy groups were subtracted from the total mass loss measured (see also SI document for calculations details).

The absorption spectra were recorded in the range of 400–900 nm with an UV-3600 Shimadzu UV-Vis-NIR spectrophotometer using 1 cm optical path length plastic cells.

Fluorescence measurements were carried out using a Fluorolog F13, Triax 320 luminescence spectrometer (Horiba Jobin Yvon, Les Ulis, France).

2.7. Cancer cell line generation and culture

Murine prostate cancer cell line RM1 was obtained from Dr. T.C. Thompson (Baylor College of Medicine, Houston, TX, USA) and Dr. M. P. Monteiro (University of Porto, Portugal). The RM1 cell line was maintained in Dulbecco's modified Eagle's medium (Invitrogen, Carlsbad, CA, USA) supplemented with 10% fetal bovine serum (Invitrogen) and 1% antimycotic-antibiotic mix (PSA, Invitrogen). The RM1 cell line was stably transfected with pcDNA6.2-CMV-Fluc [20] vector using Lipofectamine® 2000 Reagent (Invitrogen) and blasticidin (10 $\mu\text{g/mL}$, Euromedex, Souffelweyersheim, France) was used for cell line selection. Cell lines were maintained in a humidified 5% CO₂ incubator at 37 °C.

2.8. Animals handling and tumor generation

Animal manipulations were performed in agreement with French and European directives on the care and use of animals and have been approved by the local ethical committee (CEEA 50) under agreement A50120196. B6 Albino (B6N-Tyr^{c-Brd}/BrdCrCl) mice (6- to 8-week-old) were reared at the University of Bordeaux animal facilities. Animals were maintained in standard conditions under a 12-h light/dark cycle with water and food provided *ad libitum*. Animals were anesthetized with 2% isoflurane (Belamont, Nicholas Piramal Ltd, London, UK) in air. For tumor generation, cells (2.10^6 cells/100 μL) were injected subcutaneously on the right leg. Prior to the imaging session, the regions of the mice to be imaged were shaved with clippers and a depilatory cream. Each dispersion was filtered with 0.22 μm pore size membrane disks and equilibrated by dilution two times with an equal volume of PBS 2 \times before injection *via* the tail vein (160 μL , 6.25 g(SiO₂)/L). One week (7 days) after injection of RM1 cells, the four samples A, B, C and D were individually intravenously administered into 6 mice ($N = 6$, total 24 mice).

2.9. Bioluminescence imaging (BLI)

BLI was performed at Vivoptic (UMS 3767 – Univ. Bordeaux) using Lumina LT (Perkin Elmer Inc., Boston, MA, USA). Mice received an intra-peritoneal injection of D-luciferin (Promega, Madison, WI, USA; 2.9 mg in 100 μL PBS), were sedated 5 min later and images were taken at 8 min. Bioluminescence images (1 min, 4 \times 4 binning) and photographs (100 ms) were acquired successively. The bioluminescence signal was analyzed using Living Image software.

2.10. Fluorescence reflectance imaging (FRI)

FRI was performed using the Lumina LT apparatus (Perkin Elmer). Excitation was performed at 745 nm and fluorescence emission was detected with the 810–875 nm filter. A region of interest was placed on the

tumor to allow for the quantification of fluorescence signal (pH s^{-1}) using Living Image software.

2.11. Histochemistry and microscopic imaging

Tumors were fixed overnight at 4 °C with 4% paraformaldehyde, frozen and stored at −80 °C. Slices (10 μM) were then obtained and permeabilized with PBS-Triton 0.5%. Cryosections were mounted in ProLong® Gold antifade reagent with DAPI (Invitrogen). Microscopic images were acquired with the Leica DM 5000 microscope (Leica Microsystems, Wetzlar, Germany). DAPI detection was performed using an excitation filter of 340–380 nm and an emission filter of 450–490 nm. Dylight 650 fluorescence detection was performed using an excitation filter of 590–650 nm and an emission filter of 665–735 nm.

3. Results

3.1. Synthesis of aminated silica nanoparticles dually labelled with fluorescent dyes

Fluorescent dye doped silica nanoparticles were produced according to a slightly modified sol-gel procedures [21–23] in order to obtain NPs of about 15 nm diameter (Fig. 1a,b). Dually fluorescent NPs (DF-SiO₂NPs) obtained by incorporation of two dyes, DL 650 and DL 800,

were produced to enable *in vivo* optical imaging and microscopic observations of the same sample at different scales (from cellular to small animal imaging). An additional silica layer 2 ± 0.5 nm in thickness was grown around the fluorescent silica NPs (Fig. 1b,c) in order to protect of the degradation the fluorescent dyes towards further surface chemical treatments. The chemical surface modification of DF-SiO₂NPs through silanization with EDPS was performed according to an optimized method previously described [15–16]. This surface modification procedure gives a surface grafting density of 3.4 $\mu\text{mol}/\text{m}^2$ (i.e. 2 RNH₂/ nm^2) with an isoelectric point of 9.5 close to the pKa value of aminoalkyl groups (DRIFT spectra, Zeta potential measurements and TGA are shown in supplementary material document, Figs. S1,2,4). This value of IEP has been achieved due to the thermal treatment applied in a wetting solvent, the glycerol, after silanization. The condensation of polysiloxane film is completed on the surface triggering the rupture of intramolecular interactions between silanol and the amino groups.

3.2. Surface PEGylation of fluorescent silica nanoparticles and characterization

mPEG5K-ald polymer chains were characterized before grafting step. Despite the mild oxidation conditions used, we first checked if the polymer chains were fragmented. Size exclusion chromatography (SEC) was performed in aqueous medium before and after oxidation

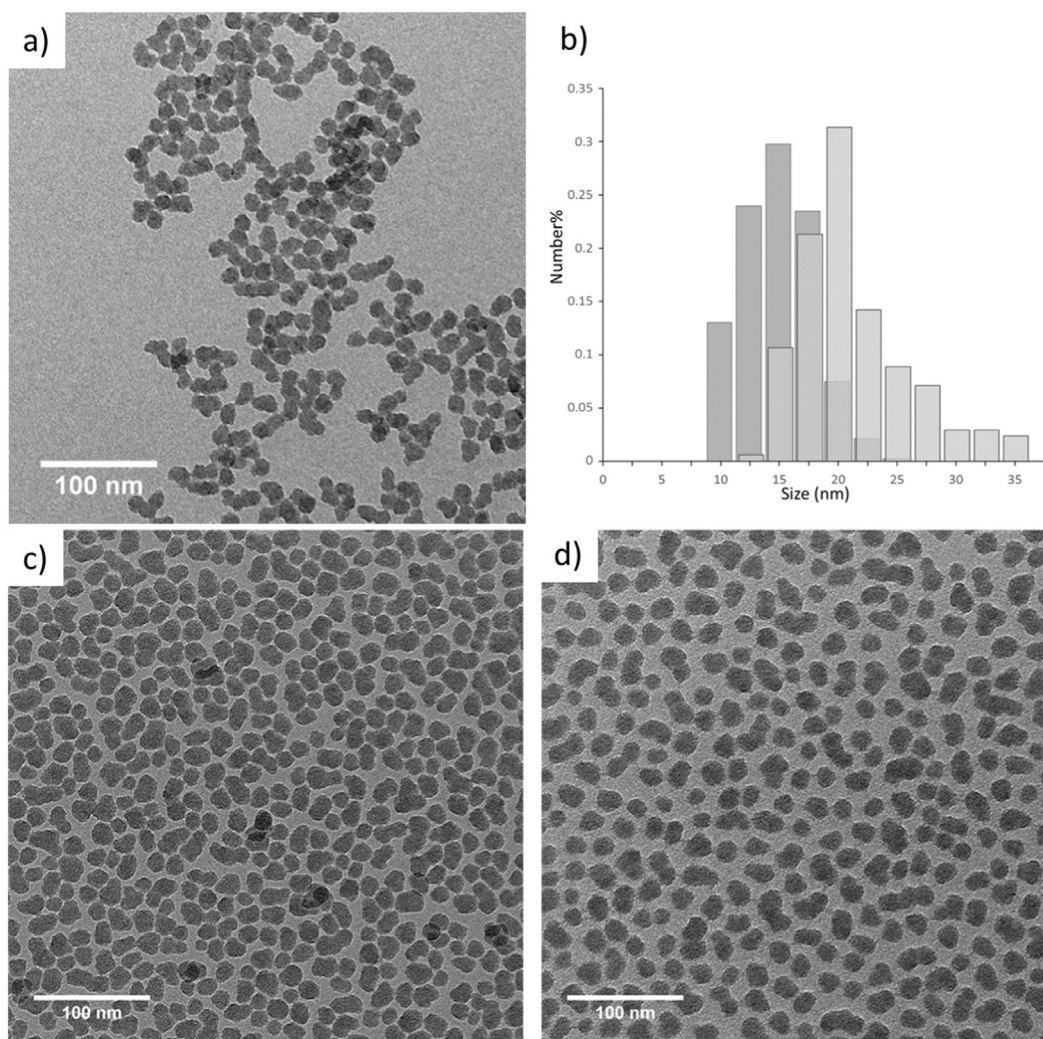


Fig. 1. TEM micrographs of a) 15 nm sized fluorescent silica cores, c) after growing with 2 nm thick silica layer and d) after PEGylation (sample A). b) Size distribution histograms of DF-SiO₂NPs before (dark grey) and after (light grey) the silica growing.

of the PEG. The announced molecular weight for commercial PEG was 5000 g/mol. We found the real Mw and thus Mn by combining with refractive index measurements in order to obtain dn/dc values: for mPEG, Mn = 5600 g/mol with a PDI (Mn/Mw) of 1.07 and for mPEG-ald, Mn = 5700 g/mol for a PDI = 1.08. It can be concluded that the polymer chains are not degraded during this chemical treatment. The slight increasing of the Mn that is in the error range can be due to the purification steps, for which smallest chains could have been removed. Then, we performed the $^1\text{H-NMR}$ on the PEG after oxidation (The spectrum and comments are shown in supplementary material). The integration of the peaks makes it possible to estimate the yield of the oxidation by taking the signal of the backbone at 3.64 ppm as reference. About 90% of the mPEG contain an aldehyde termination, so we can consider the yield of the oxidation reaction of about 90%. It can also be noticed the good coherence between the integration of H1 peaks fixed at 514 and that of H4 of the methoxy group termination, which gives about 3 protons. The NMR spectrum shows also that about 5% of mPEG chains are terminated by a methylthiomethylether moiety coming from the reaction with the DMSO, and 5% others by hydroxyl groups. These fractions do not participate to the grafting reaction and are removed during the washing steps.

DF-SiO₂NPs-EDPS were PEGylated by reductive amination between the aldehyde groups of the pre-oxidized mPEG5K molecules and primary amine functions of the NP surface. The TEM micrograph of Sample A shows increased spacing between the particles due to the presence of the polymer corona (Fig. 1d). The chemical signature of PEG molecules tethered to aminated silica NPs was evidenced by IR spectroscopy in diffuse reflectance mode on dried particles (Fig. 2) [24]. The strong IR bands at 2940 and 1342 cm⁻¹ were assigned to the asymmetrical and symmetrical (rocking and twisting) stretching modes of the alkyl chains (CH₂), respectively, while the band at 1465 cm⁻¹ was attributed to deformation vibration (δCH_2). Moreover, the band observed at 2885 cm⁻¹ can be assigned to the asymmetrical or symmetrical (rocking and twisting) stretching modes of the methyl groups (CH₃). The vibration bands from 400 to 1200 cm⁻¹ are the signature of Si—O—Si vibrations, mainly with the band at 1100 cm⁻¹ which belongs to antisymmetric stretching vibrations and the bands at 941, 801 and 469 cm⁻¹ attributed to stretching, bending and rocking vibrations. The shoulder at 1135 cm⁻¹ that appears for highest grafting levels in the middle of this broad

band may be attributed to stretching vibrations of C—O—C ether bonds. It can also be observed that the intensity of the silica bands in the spectra decreases gradually as the amount of PEG increases. All the spectra were performed with the same amount of product so this observation also confirmed by TGA analysis can be really assigned to the enrichment of PEG molecules from Sample D to A.

TGA diagrams (Fig. 3a) of DF-SiO₂NPs-PEG5K samples were performed in the same conditions (drying, weighing and thermal cycles) for a better comparison. They show a significant difference of mass losses between each level of PEGylation, from 28% for Sample D up to 47% for Sample A. Values of surface grafting density, σ , are compiled in Table 1 and presented in Fig. 1b. Regarding the evolution of the surface grafting densities as a function of the amount of PEG macromolecules, the saturation conditions are obtained for Sample A, while Sample B has a coverage of 91.5% relative to Sample A. Note that the reductive amination is quite effective in the chosen conditions since the grafting yield for the Sample D is about 50% which is quite a high value for a surface grafting reaction. Indeed, it has been showed that the reduction of aldimines with sodium borohydride carried out directly in MeOH gave the corresponding secondary amines in very high yields and very short reaction times, which makes this method very efficient when applied to substrates [25].

The conformational regimes of PEG molecules grafted on the NP surface were calculated from the values of σ obtained by TGA. The structural conformation depends on the average distance D ($D = 2(\pi\sigma)^{-1/2}$) between neighboring PEG chains [26]. When D is smaller than the Flory radius ($R_F = aN^{3/2}$, where a is the effective monomer PEG length = 0.358 nm [27], N the degree of polymerization), adjacent chains overlap and the PEG chain stretch away from the surface forming a brush layer. If $R_F/D \leq 1$, neighboring PEG molecules are not overlapped and form the mushroom conformational regime. In the present study, all the PEG layers present a brush conformational regime.

The thickness of the PEG layer was assessed using DLS measurements (Table 2). These values are determined by subtracting the hydrodynamic diameter represented by the Z-average size measured in PBS (or water see Supporting material document table S3) from the physical diameter of DF-SiO₂NPs determined by TEM observations ($R_{\text{TEM}} = 9.5$ nm). As PEG grafting density increases, compression of adjacent PEG molecules increases the hydrodynamic diameter from 45.2 for

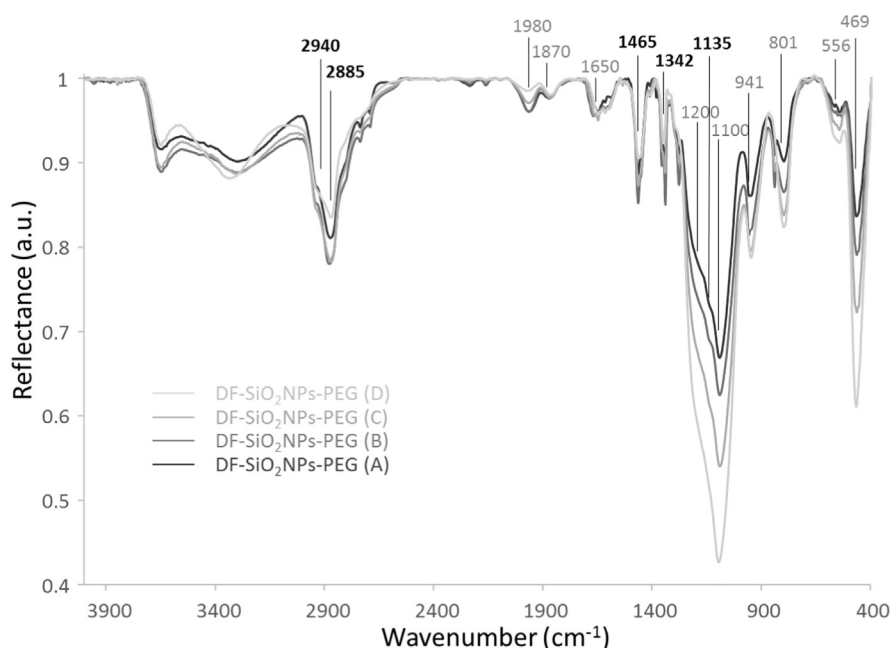


Fig. 2. Infrared spectra of PEGylated silica NPs with increasing grafting densities.

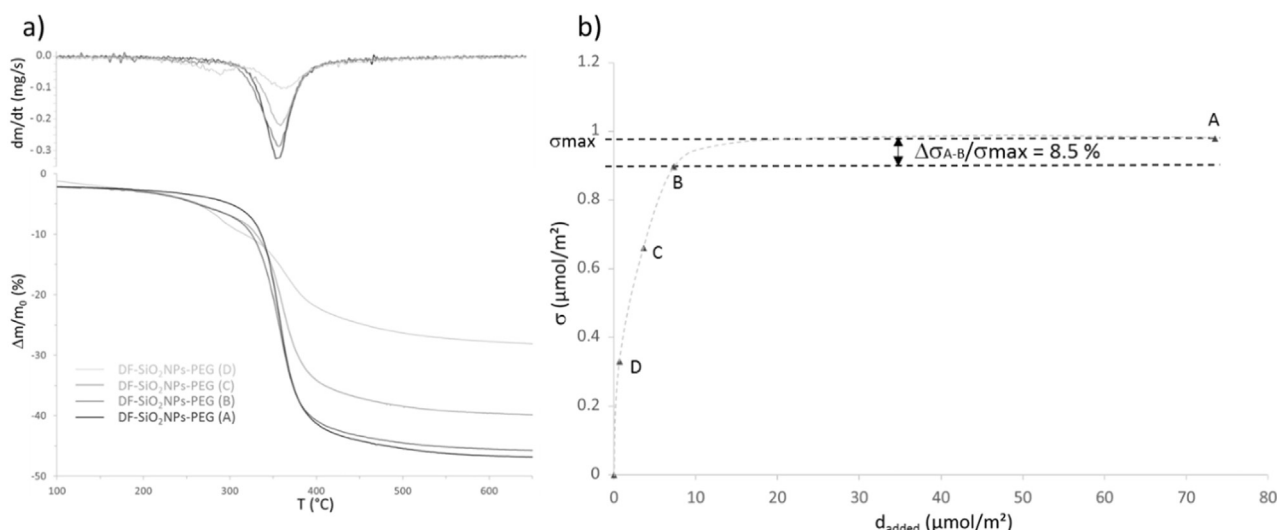


Fig. 3. a) down, TGA diagrams showing the percentual mass loss of silica nanoparticles resulting from different levels of PEGylation; up, differentiated TGA diagrams of DF-SiO₂NPs-PEG samples. b) Calculated surface grafting densities of PEG molecules (expressed in μmol/m²) from TGA assessments in function of the amount of PEG added per surface unit (d_{added}). The dashed line is just a guide for the eye.

low σ up to 50.3 nm for the higher value of σ . The thickness of the PEG layer has been initially predicted by the theoretical work of Alexander [28] and de Gennes [29] in the case of planar brushes. These pioneering works predicted a linear dependence of brush height, h , on the degree of polymerization, N : $h = aN\sigma^{*2/3}$ (a is the monomer length and $\sigma^* = \sigma l_0^2$ is the reduced grafting density [30] and l_0 the average bond length). Since then, numerous studies have considered the curvature of the surface of nanoparticles to determine the thickness of the PEG layer [30,31–34]. A generalized treatment for curved brushes was presented by Daoud and Cotton [31], who extended the phenomenological scaling arguments of Alexander and de Gennes to the somewhat related context of star polymers. This theory was extended for grafted polymers on particles by Vagberg et al. [32]. The hydrodynamic thickness L_s of the swollen brush layer on a particle of radius R is approached by the following equation:

$$L_s = \left(\frac{8N_k f^{1-\nu}}{3 \times 4^{\nu}} L_k^{\frac{1}{\nu}} + R^{\frac{1}{\nu}} \right)^{\nu} - R \quad (1)$$

where N_k is the statistical number of Kuhn segments ($N_k = n/c_{\infty}$ with n the number of chemical bonds in the macromolecule *i.e.* 3 times the degree of polymerization N and the characteristic ratio, $c_{\infty} = 4.1$ for PEG), L_k the Kuhn length ($L_k = c_{\infty} l_0$ with l_0 the average bond length = 0.147 nm for PEG), f the number of grafted chains ($f = 4\pi R^2 \sigma$) and ν , the scaling factor ($\nu = 3/5$ for good solvents). Apart from Sample D, the calculated values of L_s listed in Table 2 match quite well with those measured by DLS following the same general trend.

Table 1

Values of surface grafting density obtained by TGA analysis and corresponding conformational regimes. $N(\text{Eq.})$ is the number of equivalent of PEG used for each synthesis that takes into account the oxidation yield of mPEG (*i.e.* 90%).

Sample	$N(\text{Eq.})$	σ (mol/nm ²)	R_f (PEG-5k) (nm)	D (nm)	R_f/D	Conformational regime
Sample A	9	0.51	6.6	1.58	4.18	Brush
Sample B	0.9	0.47	6.6	1.65	4.00	Brush
Sample C	0.45	0.35	6.6	1.91	3.46	Brush
Sample D	0.09	0.18	6.6	2.66	2.48	Brush

The gap between measured and calculated values of L_s is attributed to the slight size polydispersity of NPs that can induce an overestimation of the Z-average due to the more important light scattering of bigger particles. While this model predicts a deviation of 3.4 nm in thickness of the polymer corona between samples A and D, the DLS measurements give a difference of 2.5 nm, which is a good agreement in view of the size dispersion. In mushroom regime where polymer blobs are not in interactions, the thickness L_s of the polymer layer would correspond to the Flory radius of the PEG chains. Here, in brush conformational regime, it can be observed the increasing of the thickness layer with σ , which physically corresponds to the stretching of the polymer chains that compress together when the grafting density increases.

In the aim to avoid the screening of the surface charges, zeta potential measurements were first performed in water that is a medium of low ionic strength (measured conductivity values varying from 0.04 to 0.17 mS/cm according to the measured sample) (Fig. 4). The zeta potential profile shows that the PEGylated NPs exhibit increasingly near-neutral values as the surface PEG coverage increases. Although values decrease drastically, they still remain positive due to the presence of free inner tethering amine sites and by the fact that primary amine groups are converted to secondary amines during the reaction. The presence of the polymer corona directly impacts the ζ values by moving the slipping plane away from the NP surface. In PBS, all the inner charges of the NP surface are entirely screened due to the high ionic strength and the PEGylated NPs can be considered as completely neutral.

The presence of the fluorescent dyes trapped inside the nanoparticles after PEGylation was confirmed by spectrophotometry and fluorescence spectroscopy (Fig. 5). The absorbance spectra (Fig. 5a) show the presence of both fluorophores independently of PEG density of each sample. No diffusion overlap is observed due to the small size and the colloidal stability of the dispersion. Fluorescence spectra (Fig. 5b)

Table 2

Values of hydrodynamic diameters, polydispersity indexes (PDI) and experimental and theoretical thicknesses of PEG layer obtained by Eq. (1).

Sample	DTEM(nm)	R_f (nm)	Z-Ave(PBS) (nm)	PDI	$L_{s \text{ exp}}$ (nm)	$L_{s \text{ th}}$ (nm)
Sample A	19	6.6	50.3	0.13	15.6	13.9
Sample B	19	6.6	48.8	0.16	14.9	13.6
Sample C	19	6.6	45.1	0.10	13.0	12.6
Sample D	19	6.6	45.2	0.19	13.1	10.5

display the expected values of excitation and emission maxima wavelengths showing that the dyes resisted the various chemical treatments. In these spectra it can be observed a bathochromic shift for the two fluorophores (656/677 and 792/813 nm in silica NPs, against 652/672 and 770/794 for the dyes in water). This red shift may be caused by changes in the environment of dye molecules, such as changes in polarity or polarizability. The silica matrix is not expected to change much upon increasing the dye concentration, but the number of dye molecules that are in each other vicinity increases. This leads to interactions between neighboring molecules, which lowers their excited state energy and produces a red shift in the spectra [35].

3.3. *In vivo* imaging of the EPR effect of nanoparticles in tumors

RM1-CMV-Fluc cells were injected subcutaneously on the right leg of mice ($N = 24$). One week after cell implantation, mice were first assayed for Fluc activity by BLI (Fig. 6). Nanoparticles were then injected *via* the tail vein and fluorescence distribution of the nanoparticles was monitored with FRI 1, 4, 8, 24 and 48 h after injection. Mice were separated in 4 experimental batches. The first batch of mice ($N = 6$) was injected with Sample A, the second batch ($N = 6$) with Sample B, the third batch ($N = 6$) with Sample C and the last batch ($N = 6$) with Sample D (Fig. 6).

Representative fluorescence images showed that Sample A quickly accumulated in the tumor as revealed by an increased fluorescence signal 1 h after injection; whereas for the other NPs with lower levels of PEGylation no fluorescence appeared in the tumor. In contrast, a strong accumulation of Samples B, C and D was detected in the liver just 1 h after injection. *In vivo* images showed also that the fluorescence signal resulting from nanoparticle accumulation within the tumor was much stronger for Sample A than the three other NP-batches. Time courses over 48 h of nanoparticles accumulation in the tumor and liver were represented on the graphs in Fig. 7, and corroborate that the PEGylation level of Sample A permitted a quick and strong accumulation of the nanoparticles in the tumor. The Samples B, C and D largely accumulated in the liver within 1 h while the liver uptake is drastically slower for the Sample A (Fig. 7a). Interestingly, the fluorescence intensities of the Samples B, C and D gradually decrease (by about 33% compared to the maximal accumulation values at 1 h) within 48 h, probably due to the NP degradation in the liver, in contrast to the trend in the Sample A to increase slowly for 24 h (16%). All the DF-SiO₂NPs-PEG5K samples continued to circulate during this period as evidenced by the time course of these NPs towards the tumors (Fig. 7b). The most impressive result here lies in the difference in the EPR effect uptake between Sample A and B which are distinguished by a grafting density difference of only 8.5%. The microscopy image of a tumor slice corresponding to a mouse

from Sample A (Fig. 8) shows the fluorescence of DL650 attesting the presence of the NPs all around tumor cells. Even if further characterization has to be performed to determine the precise location of the NPs inside or outside the cells, these dually labelled NPs are obviously good candidates for this type of study at multiple scales using different imaging techniques.

4. Discussion

In the aim of studying the impact of slight variations in the surface grafting density of PEG molecules in the brush regime on the tumor uptake by EPR effect, we chose PEG coatings with R_F/D ratio around 2.8. This value represents a threshold corresponding to a dense brush conformational regime beyond which it has been observed an effective stealth behavior of PEGylated 100 nm polystyrene NPs against human monocytic THP-1 cells *in vitro* [14]. We preferred also in this study a NP size of around 20 nm (without the outer PEG layer), too big to be cleared by renal excretion [36] and small enough to decrease the macrophage uptake [13]. We used a single PEG molecular weight typically of 5000 g/mol (Mn 5700 g/mol, PDI 1.08) that displays a good ability to decrease protein adsorption onto the NP surfaces [13,37–39]. These PEG molecules were first functionalized by aldehyde groups before grafting on surface chemically modified silica NPs. The chemical surface modification previously optimized on silica nanoparticles [16] allows a control over the grafting rate in order to generate several samples of different R_F/D ratios of 2.48, 3.46, 4.00 and 4.18. Light in the visible-wavelength range is routinely used for conventional and intravital microscopy [40] but emission spectra within the near infrared (NIR) window (700–900 nm) must be used for deep *in vivo* imaging because of absorption and tissue autofluorescence [41]. The dual doping of silica NPs described in the present work enabled their tracking *in vivo* by FRI by using DL 800 wavelength in the near infra-red (NIR) windows and microscopic imaging *in vitro* using DL 650. RM1 cells provided rapidly growing tumors in immunocompetent mice including subcutaneous, orthotopic and metastasis [42]. In the present work, subcutaneous tumors were generated at the same time and tumor growth was further followed by individual BLI measurement ensuring homogeneity between the experimental series when mice were injected with NPs. Although FRI did not provide absolute quantification, it allowed the monitoring of NP accumulation in both subcutaneous tumors and in the liver. FRI clearly discriminated NP behavior *in vivo* according to PEG status.

Despite the fact that all the PEGylated NPs are in the brush conformational regime, they do not suffer the same fate *in vivo*. A rapid accumulation in the liver was expected for NPs displaying a R_F/D under the threshold value of 2.8, but less expected for PEGylated NPs with values of 3.46 and 4.00. For $R_F/D = 3.46$ and 4.00 the uptake by the EPR effect increase gradually but remain reduced due to the rapid extravasation by the liver. For $R_F/D = 4.18$, an increase of fluorescence in tumor as well as in liver was observed for up to 24 h. In this case the intensity of tumor fluorescence approximately corresponds to the fluorescence observed in the liver which means that this level of PEGylation enables an important percentage of these NPs to evade the RES. The most surprising outcome is the huge difference in biodistribution kinetics between Samples A and B whose main difference results from a slight change of PEG coverage, a difference of 8.5%. The NPs used in this study presented a more elevated curvature than those used in the previous report of Lai et al. [14] and it seems also possible that the R_F/D threshold is shifted from 2.8 to about 4. Indeed, Chan et al. observed on gold nanoparticles of sizes varying from 15 to 90 nm, that under fixed PEG grafting density, decreasing nanoparticles size increases plasma protein absorption [13]. Highly curved surfaces impact the intermolecular PEG-PEG interactions within the polymer corona. The molecules tend to spread out in the volume gained away from the convex surface which lowers the thermodynamic barrier to opsonisation and thus, affects the threshold value.

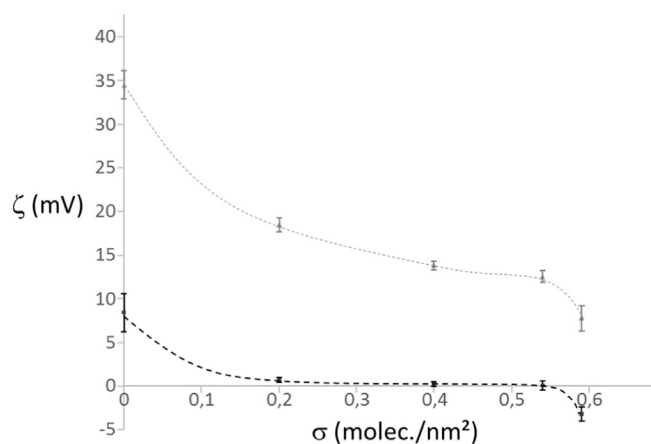


Fig. 4. Zeta potential profiles of PEGylated silica NPs in water (light grey) and PBS buffer (dark grey) vs increasing surface grafting densities of PEG molecules. The dashed lines are just guides for the eye.

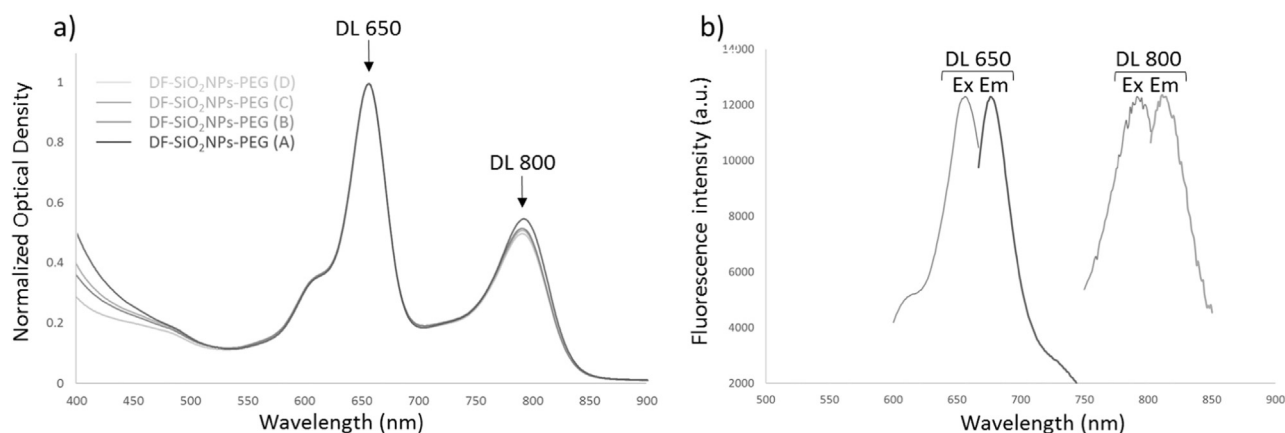


Fig. 5. a) Absorbance spectra of dually fluorescent silica nanoparticles after PEGylation. b) fluorescence spectre of DF-SiO₂NPs-PEG (A) sample ($\lambda_{\text{EX}}/\lambda_{\text{EM}}$ 656/677 nm and $\lambda_{\text{EX}}/\lambda_{\text{EM}}$ 792/813 nm).

The hydrodynamic diameters of Samples A and B and the PEG volume fractions represent 94 and 93.7% of the overall NP volume respectively. The saturation of surface was reached by applying a 10-fold excess of PEG relative to Sample B in a very concentrated PEG medium (358 g/L, ~30% v/v) which results in a gain of 8.5% in terms of surface grafting density. Although monodisperse macromolecules are certainly close together, with such excess, there may be small chains in the environment that can fill vacant spaces between the larger chains without really affecting the thickness values. Furthermore, this slight variation of 8.5% implies a difference in the structuration of the PEG layer between both NPs, which materializes in the formations of gaps by overlapping neighboring chains, entanglements, and many spatial configurations over very short time intervals [43]. Moreover, the NP environment, that is the blood, is composed of over 3000 different proteins

[44] representing an overall concentration of 60 g/L. These proteins are capable of interacting with the underlying NP surface where free ammonium sites remain. Neighboring proteins can immediately exploit any space formed in the molecular layer leading to opsonisation. This structuration of the PEG layer influences the composition and thickness of the protein corona which have been demonstrated to have a deep impact on the biological fate of PEGylated NPs [13,14,45,46]. The structure of the stealth polymer layer can determine the type of plasma protein. Even in some cases, it has been demonstrated that clusterin, a plasma protein named also apolipoprotein J, has been shown to adsorb on PEGylated 100 nm polymer NPs. This plasma protein can reduce non-specific cellular uptake and assists the stealth effect [47]. Tenzer et al. observed differences in the composition of the protein corona between silica nanoparticles of 8 nm, 20 nm and 125 nm [48]. Indeed, the

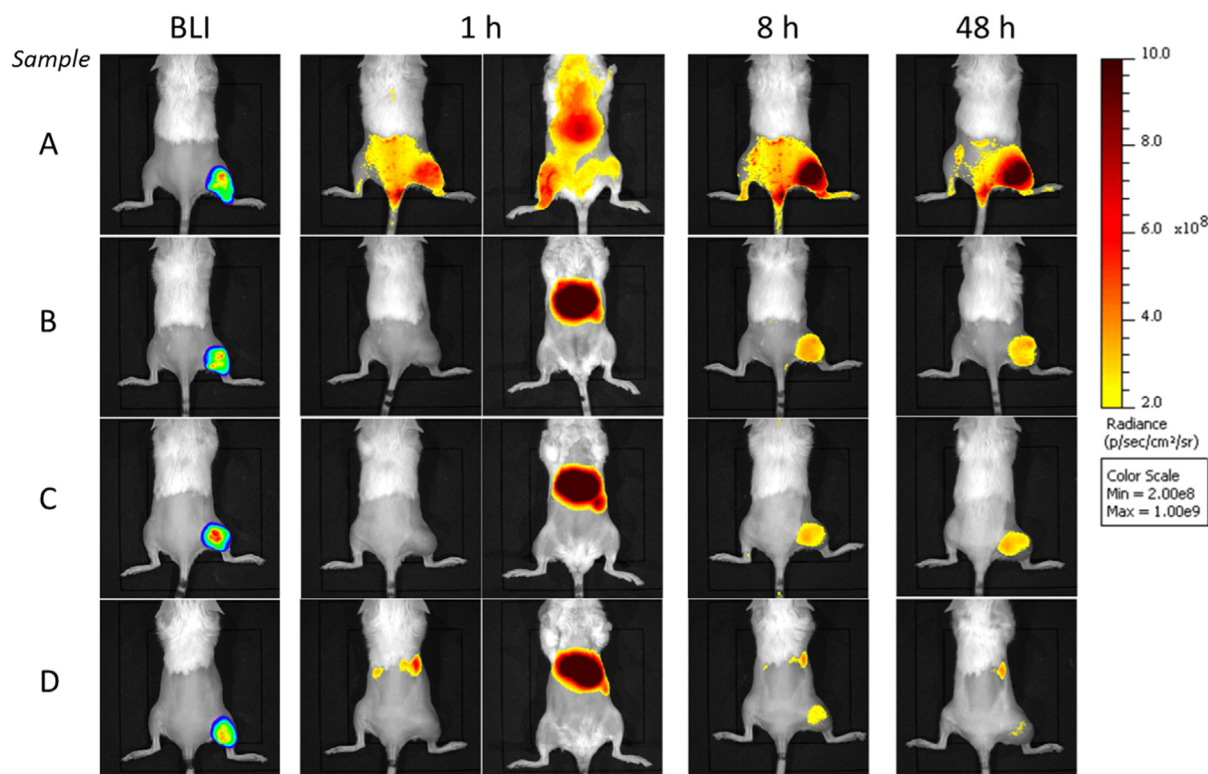


Fig. 6. BLI (prone position) and FRI of a representative mouse from batch A, batch B, batch C and batch D injected with corresponding DF-SiO₂NPs-PEG5k (samples A, B, C and D) observed at 1 h (right, prone position; left, supine position), 8 h and 48 h (prone position).

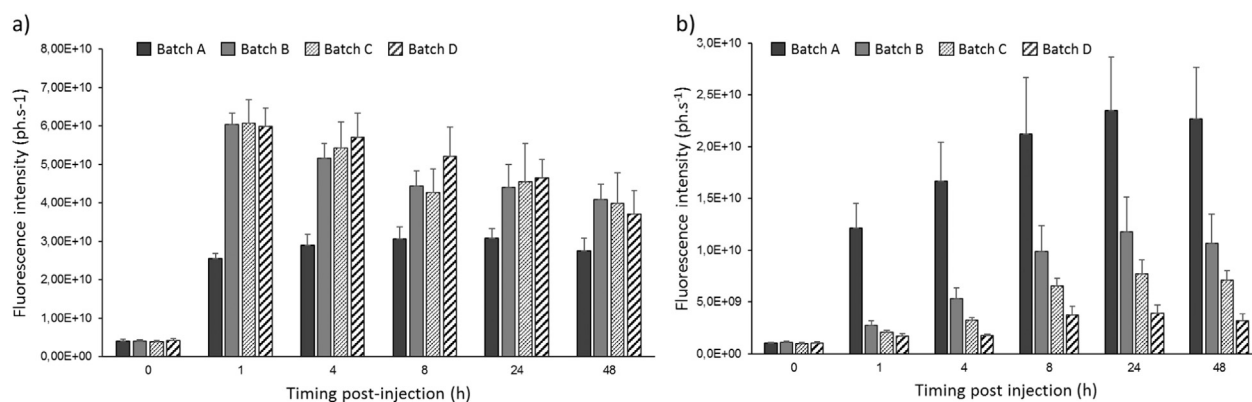


Fig. 7. Time courses of DF-SiO₂NPs-PEG5k (samples A, B, C and D) accumulation: a) into the liver, b) into the tumors of mice bearing RM1 subcutaneous tumors ($N = 6$ for each batch).

curvature radius affects the contact surface between the nanoparticle and the biomolecule, which induces differences in affinity. The curvature radius also affects the level of conformational changes of adsorbed proteins [49].

The results of our experiments suggest that small NPs with highly curved surfaces are much more sensitive to slight variations of PEG surface grafting density with respect to RES clearance. The intermolecular spacing generated by a high radius of curvature must be compensated by high grafting densities through a saturated polymer layer. When their surface grafting density is sufficiently high, dually fluorescent silica nanoparticles have shown their ability to label the EPR effect in mice bearing tumors with longer blood circulation times up to 24 h. Our results underscore the need to thoroughly control the surface chemistry and the PEG grafting density on small nanoparticles to achieve dense brush regimes as a prerequisite to passive tumor targeting and before designing targeting strategies. In this study, the control of the conjugation was achieved by the combination of functionalized nanoparticles offering a large number of accessible functions with an anchoring reaction of high yield in a good PEG solvent. Such PEGylated fluorescent NPs could be valuable labels to detect and assess the magnitude of the tumor EPR effect.

Transparency document

The Transparency document associated with this article can be found, in the online version.

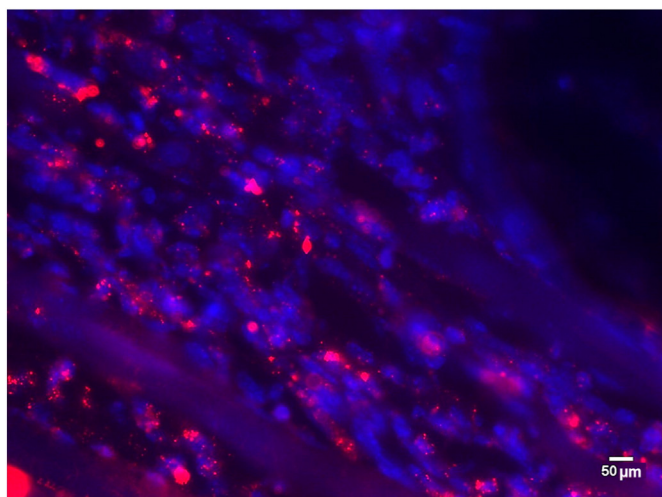


Fig. 8. Microscopy image of a tumor slice from a mouse injected 48 h after with sample A. Blue staining (DAPI) evidences nuclei cells while red color is due to the fluorescence of DL650 of the NP.

Acknowledgement

We thank Dr. Pierre Costet and Laetitia Medan from Univ. Bordeaux animal's facilities service for the animals' care. The authors are also grateful to Dr. Olivier Sandre and Amélie Vax of the Laboratory of Organic Polymer Chemistry (LCPO) for DLS, SEC measurements, and fruitful discussions; to Dominique Denux and Philippe Dagault of the Bordeaux's Institute of Condensed matter Chemistry (ICMCB) for TG analysis and to Dr. Claire Mazzocco (EA IMOTION) for cell line engineering. Laurent Adumeau was a recipient of a scholarship from the French Ministry of Education and Research. This work was supported by Labex TRAIL (ANR-10-LABX-57).

Appendix A. Supplementary data

Supplementary data to this article can be found online at <http://dx.doi.org/10.1016/j.bbagen.2017.01.036>.

References

- [1] W.R. Sanhai, J.H. Sakamoto, R. Canady, M. Ferrari, Seven challenges for nanomédecine, *Nat. Nanotechnol.* 3 (2008) 242–244.
- [2] N. Bertrand, J. Wu, X. Xu, N. Kamaly, O.C. Farokhzad, Cancer nanotechnology: the impact of passive and active targeting in the era of modern cancer biology, *Adv. Drug Deliv. Rev.* 66 (2014) 2–25.
- [3] L. Brannon-Peppas, J.O. Blanchette, Nanoparticles and targeted systems for cancer therapy, *Adv. Drug Deliv. Rev.* 56 (2004) 1649–1659.
- [4] X.-Q. Zhang, X. Xu, N. Bertrand, E. Pridgen, A. Swami, O.C. Farokhzad, Interactions of nanomaterials and biological systems: implications to personalized nanomedicine, *Adv. Drug Deliv. Rev.* 64 (2012) 1363–1384.
- [5] P. Opanasopit, M. Nishikawa, M. Hashida, Factors affecting drug and gene delivery: effects of interaction with blood components, *Crit. Rev. Ther. Drug Carrier Syst.* 19 (2002) 191–233.
- [6] S.D. Li, L. Huang, Pharmacokinetics and biodistribution of nanoparticles, *Mol. Pharm.* 5 (2008) 496–504.
- [7] S. Nie, Understanding and overcoming major barriers in cancer nanomedicine, *Nanomedicine* 5 (2010) 523–528.
- [8] R. Gref, A. Domb, P. Quellec, T. Blunk, R.H. Muller, J.M. Verbavatz, R. Langer, The controlled intravenous delivery of drugs using PEG-coated sterically stabilized nanoparticles, *Adv. Drug Deliv. Rev.* 16 (1995) 215–233.
- [9] A. Vonarbourg, C. Passirani, P. Saulnier, J.P. Benoit, Parameters influencing the stealthiness of colloidal drug delivery systems, *Biomaterials* 27 (2006) 4356–4373.
- [10] F. Alexis, E. Pridgen, L.K. Molnar, O.C. Farokhzad, Factors affecting the clearance and biodistribution of polymeric nanoparticles, *Mol. Pharm.* 5 (2008) 505–515.
- [11] J.V. Jokerst, T. Lobovkina, R.N. Zare, S.S. Gambhir, Nanoparticle PEGylation for imaging and therapy, *Nanomedicine (London)* 6 (2011) 715–728.
- [12] J.L. Suk, Q. Xu, N. Kim, J. Hanes, L.M. Ensign, PEGylation as a strategy for improving nanoparticle-based drug and gene delivery, *Adv. Drug Deliv. Rev.* 99 (2016) 28–51.
- [13] C.D. Walkey, J.B. Olsen, H. Guo, A. Emili, W.C.W. Chan, Nanoparticle size and surface chemistry determine serum protein adsorption and macrophage uptake, *J. Am. Chem. Soc.* 134 (2012) 2139–2147.
- [14] Q. Yang, S.W. Jones, C.L. Parker, W.C. Zamboni, J.E. Bear, S.K. Lai, Evading immune cell uptake and clearance requires PEG grafting at densities substantially exceeding the minimum for brush conformation, *Mol. Pharm.* 11 (2014) 1250–1258.
- [15] S. Mornet, J. Portier, E. Duguet, A method for synthesis and functionalization of ultra-small superparamagnetic covalent carriers based on maghemite and dextran, *J. Magn. Mater.* 293 (2005) 127–134.

- [16] N. Reinhardt, L. Adumeau, O. Lambert, S. Ravaine, S. Mornet, Quaternary ammonium groups exposed at the surface of silica nanoparticles suitable for DNA complexation in the presence of cationic lipids, *J. Phys. Chem. B* 119 (2015) 6401–6411.
- [17] K.E. Pfützner, J.G. Moffatt, A new and selective oxidation of alcohols, *J. Am. Chem. Soc.* 85 (1963) 3027–3028.
- [18] G. Tojo, M. Fernandez, in: G. Tojo (Ed.), *Oxidation of Alcohols to Aldehydes and Ketones, a Guide of Common Practice*, Book Chapter, Springer Science and Business Media, Inc., New York 2006, pp. 97–179.
- [19] P.-U. Park, S.-N. Kim, W.-H. Choi, H.-S. Jang, G.-S. Lee, S.-C. Kwon, Method for Preparing High-purity Polyethyleneglycol Aldehyde Derivatives, US8349969 B2, January 8, 2013.
- [20] C. Mazzocco, G. Fracasso, C. Germain-Genevois, N. Dugot-Senant, M. Figini, M. Colombatti, N. Grenier, F. Couillaud, In vivo imaging of prostate cancer using an anti-PSMA scFv fragment as a probe, *Sci. Report.* 6 (2016) 23314.
- [21] W. Stöber, A. Fink, E. Bohn, Controlled growth of monodisperse silica spheres in the micron size range, *J. Colloid Interface Sci.* 26 (1968) 62–69.
- [22] A.V. Blaaderen, A. Vrij, Synthesis and characterization of colloidal dispersions of fluorescent, monodisperse silica spheres, *Langmuir* 8 (1992) 2921–2931.
- [23] D.R. Larson, H. Ow, H.D. Vishwasrao, A.A. Heikal, U. Wiesner, W.W. Webb, Silica nanoparticle architecture determines radiative properties of encapsulated fluorophores, *Chem. Mater.* 20 (2008) 2677–2684.
- [24] R.M. Silverstein, F.X. Webster, D.J. Kiemle, *Spectrometric identification of organic compounds*, seventh ed. John Wiley & sons, New York, NY, 2005.
- [25] A.F. Abdel-Magid, K.G. Carson, B.D. Harris, C.A. Maryanoff, R.D. Shah, Reductive amination of aldehydes and ketones with sodium triacetoxyborohydride. Studies on direct and indirect reductive amination procedures, *J. Org. Chem.* 61 (1996) 3849–3862.
- [26] P.G. De Gennes, Polymers at an interface; a simplified view, *Adv. Colloid Interf. Sci.* 27 (1987) 189–209.
- [27] M.A. Rixman, D. Dean, C. Ortiz, Nanoscale intermolecular interactions between human serum albumin and low grafting density surfaces of poly(ethylene oxide), *Langmuir* 19 (2003) 9357–9372.
- [28] S. Alexander, Adsorption of chain molecules with a polar head a scaling description, *J. Phys. France* 38 (1977) 983–987.
- [29] P.G. de Gennes, Conformations of polymers attached to an interface, *Macromolecules* 13 (1980) 1069–1075.
- [30] D. Dukes, Y. Li, S. Lewis, B. Benicewicz, L. Schadler, S.K. Kumar, Conformational transitions of spherical polymer brushes: synthesis, characterization, and theory, *Macromolecules* 43 (2010) 1564–1570.
- [31] M. Daoud, J.P. Cotton, Star shaped polymers: a model for the conformation and its concentration dependence, *J. Phys. France* 43 (1982) 531–538.
- [32] L.J.M. Vagberg, K.A. Cogan, A.P. Gast, Light-scattering study of starlike polymeric micelles, *Macromolecules* 24 (1991) 1670–1677.
- [33] K. Ohno, T. Morinaga, S. Takeno, Y. Tsujii, T. Fukuda, Suspensions of silica particles grafted with concentrated polymer brush: effects of graft chain length on brush layer thickness and colloidal crystallization, *Macromolecules* 40 (2007) 9143–9150.
- [34] E.M. Sevick, Shear swelling of polymer brushes grafted onto convex and concave surfaces, *Macromolecules* 29 (1996) 6952–6958.
- [35] A. Imhof, M. Megens, J.J. Engelberts, D.T.N. de Lang, R. Sprik, W.L. Vos, Spectroscopy of fluorescein (FITC) dyed colloidal silica spheres, *J. Phys. Chem. B* 103 (1999) 1408–1415.
- [36] H.S. Choi, W. Liu, P. Mistra, E. Tanaka, J.P. Zimmer, B. Itty Ipe, G.M. Bawendi, J.V. Frangioni, Renal clearance of quantum dots, *Nat. Biotechnol.* 25 (2007) 1165–1170.
- [37] R. Gref, M. Luck, P. Quellec, M. Marchand, E. Dellacherie, S. Harnisch, T. Blunk, R.H. Muller, 'Stealth' corona-core nanoparticles surface modified by polyethylene glycol (PEG): influences of the corona (PEG chain length and surface density) and of the core composition on phagocytic uptake and plasma protein adsorption, *Colloids Surf. B: Biointerfaces* 18 (2000) 301–313.
- [38] A. Mori, A.L. Klivanov, V.P. Torchilin, L. Huang, Influence of the steric barrier activity of amphipathic poly(ethylene glycol) and ganglioside GM1 on the circulation time of liposomes and on the target binding of immunoliposomes in vivo, *FEBS Lett.* 284 (1991) 263–266.
- [39] Q. Dai, C. Walkey, W.C.W. Chan, Polyethylene glycol backfilling mitigates the negative impact of the protein corona on nanoparticle cell targeting, *Angew. Chem. Int. Ed.* 53 (2014) 5093–5096.
- [40] E.B. Brown, R.B. Campbell, Y. Tsuzuki, L. Xu, P. Carmeliet, D. Fukumura, R.K. Jain, In vivo measurement of gene expression, angiogenesis and physiological function in tumors using multiphoton laser scanning microscopy, *Nat. Med.* 7 (2001) 864–868.
- [41] R. Weissleder, V. Ntziachristos, Shedding light onto live molecular targets, *Nat. Med.* 9 (2003) 123–128.
- [42] C.A. Power, H. Pwint, J. Chan, J. Cho, Y. Yu, W. Walsh, P.J. Russell, A novel model of bone-metastatic prostate cancer in immunocompetent mice, *Prostate* 69 (2009) 1613–1623.
- [43] C. Jeppesen, J.Y. Wong, T.L. Kuhl, J.N. Israelachvili, N. Mullah, S. Zalipsky, C.M. Marques, Impact of polymer tether length on multiple ligand-receptor bond formation, *Science* 293 (2001) 465–468.
- [44] N.L. Anderson, N.G. Anderson, The human plasma proteome: history, character, and diagnostic prospects, *Mol. Cell. Proteomics* 1 (2002) 845–867.
- [45] C. Sacchetti, K. Motamedchaboki, A. Magrini, G. Palmieri, M. Mattei, G. Bernardini, N. Rosato, N. Bottini, M. Bottini, Surface PEG conformation influences the protein corona of polyethylene glycol-modified single-walled carbon nanotubes: potential implications on biological performance, *ACS Nano* 7 (2013) 1974–1989.
- [46] S. Tenzer, D. Docter, J. Kuharev, A. Musyanovych, V. Fetz, R. Hecht, F. Schlenk, D. Fischer, K. Kiouptsi, C. Reinhardt, K. Landfester, H. Schild, M. Maskos, S.K. Knauer, R.H. Stauber, Rapid formation of plasma protein corona critically affects nanoparticle pathophysiology, *Nat. Nanotechnol.* 8 (2013) 772–781.
- [47] S. Schöttler, G. Becker, S. Winzen, T. Steinbach, K. Mohr, K. Landfester, V. Mailänder, F.R. Wurm, Protein adsorption is required for stealth effect of poly(ethylene glycol)- and poly(phosphoester)-coated nanocarriers, *Nat. Nanotechnol.* 11 (2016) 372–377.
- [48] S. Tenzer, D. Docter, S. Rosfa, A. Wlodarski, J. Kuharev, A. Rekić, S.K. Knauer, C. Bantz, T. Nawroth, C. Bier, J. Sirirattanapan, W. Mann, L. Treuel, R. Zellner, M. Maskos, H. Schild, R.H. Stauber, Nanoparticle size is a critical physicochemical determinant of the human blood plasma corona: a comprehensive quantitative proteomic analysis, *ACS Nano* 5 (2011) 7155–7167.
- [49] C.D. Walkey, W.C.W. Chan, Understanding and controlling the interaction of nanomaterials with proteins in a physiological environment, *Chem. Soc. Rev.* 41 (2012) 2780–2799.